https://doi.org/10.15407/ujpe71.7.597

A.V. LYSYTSYA,[1] V.O. MYSLINCHUK,[1] M.V. MOROZ,[2] B.D. NECHYPORUK,[1] B.P. RUDYK,[2] S.V. VIRKO[3]

[1] Rivne State University of Humanities
(31, Plastova Str., Rivne 33028, Ukraine)
[2] National University of Water and Environmental Engineering
(11, Soborna Str., Rivne 33028, Ukraine)
[3] V.E. Lashkaryov Institute of Semiconductor Physics, Nat. Acad. of Sci. of Ukraine
(45, Nauky Ave., Kyiv 03028, Ukraine)

FABRICATION AND PHYSICAL PROPERTIES OF MAGNETITE AND ZINC FERRITE

The possibility of producing magnetite and zinc ferrite nanocrystals using the electrolytic method has been studied. The synthesis of nanoparticles occurred in an electrolyzer with Fe or Fe + Zn electrodes immersed in an aqueous solution of NaCl. X-ray diffraction (XRD) studies were applied to determine the composition of the obtained specimens, the nanocrystal sizes, and the crystal lattice parameters. The nanocrystal sizes were calculated using the Debye–Scherrer formula, the Williamson–Hall method, and the dimensional deformation method. It was shown that the application of iron electrodes leads to the formation of magnetite nanocrystals, whereas the combination of iron and zinc electrodes results in the appearance of the "zinc ferrite–zinc oxide" system. Analysis of the Raman spectra of the studied specimens confirmed the XRD results.

Keywords: magnetite, zinc ferrite, XRD, nanoparticle size, Debye–Scherrer formula, Williamson–Hall method, crystal lattice parameter, Raman scattering.

1. Introduction

According to their magnetic properties, all substances are classified into three main types: diamagnetics, paramagnetics, and ferromagnetics. Among those substances, ferromagnetics have found the most widespread application. They are used to construct magnetic circuits in electrical machines, such as transformers, DC and AC machines, devices for recording, storing, and reproducing information, *etc.* Ferromagnetic materials include iron, nickel, chromium, rare earth elements, their alloys and oxides, as well as natural iron-based minerals, in particular, magnetite [1].

Among ferromagnetics, a special class of materials, ferrites, has to be distinguished. They differ from ordinary metallic ferromagnets by their high electrical resistance. Today, hundreds of various ferrite brands are known, which are different in chemical composition, crystal structure, and magnetic, optical, and other properties. Besides single-component ferrites, two- and multicomponent ferrites have been widely used, and the areas of their application are permanently expanding. Most ferrites possess magnetic properties even at high temperatures; in addition, they have high resistivity and low dielectric losses. Ferrites that crystallize in the spinel structure, and the chemical formula of which is $Me\mathrm{Fe_2O_4}$, where

Citation: Lysytsya A.V., Myslinchuk V.O., Moroz M.V., Nechyporuk B.D., Rudyk B.P., Virko S.V. Fabrication and physical properties of magnetite and zinc ferrite. *Ukr. J. Phys.* **71**, No. 7, 597 (2026). https://doi.org/10.15407/ujpe71.7.597.

Me denotes the cations Fe, Co, Ni, Zn, and others, comprise a very important group of magnetic materials. They are a universal material that ensures the stable and efficient operation of electronic components in a wide spectral interval of electromagnetic radiation, ranging from long-wave to microwave technology [2].

Nowadays, interest in ferromagnetic materials has increased due to the possibility of obtaining them in a nanostructured form and, as a result, the expansion of the scope of their application in technology, medicine, biology, ecology, and so forth [3–5]. In particular, one of the most complicated environmental problems is the pollution of water resources. Among many harmful compounds formed as a result of anthropogenic activity, there are dyes from the textile, paper, leather, cosmetic, plastic, and food industries. Dyes used for dyeing textiles, leather, and paper have an adverse effect on the environment. Their removal from water basins and wastewater treatment are rather complicated tasks. Therefore, there is a permanent search for effective materials to purify water resources from the aforementioned dyes. Magnetite (Fe_3O_4) is a promising candidate for water purification, since it is non-toxic, has a large surface area-to-volume ratio, high adsorption capacity, and high photostability. It can be easily doped with metals, including zinc, for biomedical or environmental applications, in particular, for the removal of phenol, ketoprofen, methylene blue, methyl orange, Congo red dye, rhodamine B, and Hg(II) and Th(IV) ions. In addition, the magnetic properties of iron oxide can facilitate the removal of nanoparticles with adsorbed pollutants from aqueous suspensions using an external magnetic field [6].

When the size of magnetic particles is reduced to the nanometer scale, their surface area-to-volume ratio increases substantially, which leads to the emergence of new properties that radically distinguish nanoparticles from bulk materials. In particular, this is the manifestation of superparamagnetism, magnetic quantum tunneling, and the appearance of spin-glass-like behavior. Those properties of magnetic nanoparticles determine their versatile technological applications, including magnetic data storage, the creation and application of ferromagnetic liquids, medical imaging, targeted drug delivery, catalysis, and others. In particular, in Ref. [7], using zinc ferrite, $ZnFe_2O_4$, as an example, striking changes in its magnetic properties with the reduction of the grain size to the nanometer scale were demonstrated.

From an ecological viewpoint, a challenging issue is the purification of enterprises' wastewater from phenol. Magnetite nanoparticles demonstrate a certain adsorption capacity with respect to phenolic compounds, for example, in Fe_3O_4-coated nanofibrils [8]. In a photocatalytic process using superparamagnetic iron oxide nanoparticles (SPIONs, Fe_2O_4), 94.9% phenol removal was achieved under optimized conditions (pH = 3, an initial phenol concentration of 80 mg/l, the ratio UV/SPIONs = 3, and a contact time of 60 min) [9]. This result highlights the potential of magnetite in light-activated pathways of phenol degradation. Furthermore, Fe_3O_4 nanoparticles, when used as a heterogeneous Fenton catalyst, have demonstrated exceptional efficiency by achieving 100% phenol removal and a 70% reduction in the chemical oxygen demand (COD) under optimized conditions within a wide pH range (2–9) [10]. At the same time, modified Fe_3O_4 hydrogel nanoparticles provided 98% phenol removal and an 80% reduction of COD after 180 min, with good stability ($\geq$ 55% of COD removal efficiency after three cycles) [11].

Ferrite nanoparticles do not have their own permanent magnetic field in the absence of an external field, so they are prevented from clumping into aggregates due to magnetic interaction. This is an important characteristic for biomedical applications, for example, when transporting drugs through small-diameter blood vessels, where particle aggregation is extremely undesirable [12]. In particular, in targeted drug delivery, their magnetic properties allow the precise delivery of biologically active substances to specific locations in the body [13]. In cancer therapy, the hyperthermia treatment is used, in which iron oxide nanoparticles generate heat under the action of an external magnetic field to destroy cancer cells [14].

The aim of this work is to obtain magnetite and zinc ferrite nanocrystals using the electrolytic method and to study their physical properties.

2. Experimental Part

Magnetite nanocrystals and nanocrystals of the zinc ferrite–zinc oxide system were obtained by means of the electrolytic method in an open glass electrolytic cell. The electrolyte was a solution of sodium chloride (NaCl) in distilled water. The concentration of NaCl

in the electrolyte was 5.8 g/l. A stabilized, regulated DC source was used to power the electrolyzer. The synthesis was carried out at a constant electrolyte temperature, which varied from room temperature to 100°C in various series of experiments. Iron electrodes were used to synthesize magnetite, and iron and zinc electrodes were used to obtain nanocrystals of the "zinc ferrite–zinc oxide" system. The duration of the nanocrystal synthesis process was 3 h, and the current density was 26×10^{-2} A/cm^2. To ensure uniform consumption of electrode material, the DC direction was reversed every 30 min. After the termination of electrolysis, the electrolyte was filtered using a paper filter, and the resulting powder was washed with a fivefold volume of distilled water. The specimens were dried in air at room temperature. For the nomenclature of experimental specimens, see Table 1.

The Raman scattering (RS) spectra of the studied specimens were studied in the backscattering geometry at room temperature. The experimental spectra were registered on an MDR-23 spectrometer equipped with a DU-401 CCD camera (Andor, UK). The excitation source for the Raman spectra was laser emission with a wavelength of 457 nm (Diode Pumped Solid State Laser, by CNI Laser). X-ray diffraction studies were carried out on a DRON-4 diffractometer using CuK_α radiation at room temperature. The diffractograms were scanned following the Bragg–Brentano ($\theta - 2\theta$) scheme. The anode voltage and the current were 41 kV and 21 mA, respectively. The diffractogram scanning step was 0.05°, and the exposure time was 5 s.

The mathematical treatment of experimental diffractograms was carried out by describing every experimental reflex as a Gaussian function. As a result, information was obtained about the angular position 2θ, the half-width (the width at half height) β, and the integral intensity I. The obtained results were used to interpret the experimental diffractograms, determine the crystal lattice parameters, and calculate the sizes of nanocrystals. The Raman spectra were treated similarly, but using the Cauchy–Lorentz function.

3. Measurement Results and Their Discussion

In Fig. 1, experimental diffractograms are shown for specimens obtained using the electrolytic method with a sodium chloride solution as the electrolyte at various synthesis temperatures and various electrode combinations. It was suggested that during the electrolytic synthesis, the specimens can contain iron oxides and hydroxides if iron electrodes are used, and zinc oxide and zinc ferrite if iron and zinc electrodes are used simultaneously. To verify this hypothesis, the angular positions of the reflections belonging to iron, its oxides and hydroxides, and zinc ferrite were calculated using the known interplanar distances and the Wolf–Bragg formula [15]

$$2d \sin\theta = k\lambda,$$

where d is the interplanar distance, θ is the diffraction angle, k is the order of the diffraction maximum, and λ is the wavelength of the X-ray radiation.

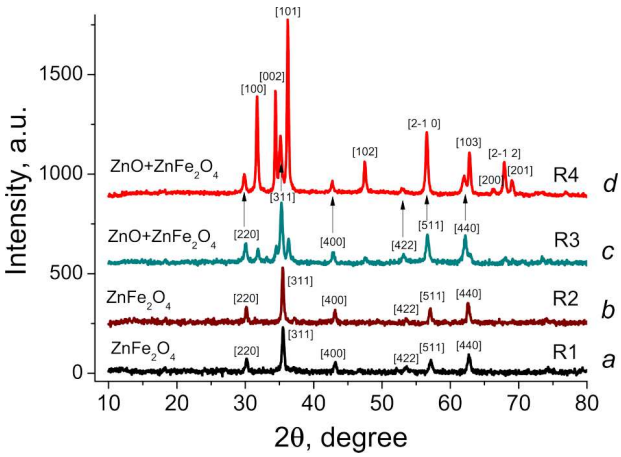

Fig. 1. X-ray diffraction patterns of specimens synthesized using the electrolytic method: (a) specimen R1, zinc ferrite, $t = 20$ °C, Fe electrodes; (b) specimen R2, zinc ferrite, $t =$ $= 93$ °C, Fe electrodes; (c) specimen R3, "zinc ferrite–zinc oxide" system, $t = 93$ °C, Fe + Zn electrodes; (d) specimen R4, "zinc ferrite–zinc oxide" system, $t = 93$ °C, Fe + Zn electrodes, the area of zinc electrode is larger than for specimen R3. The following reflections are shown: (a, b, c) zinc ferrite, (d) zinc oxide

Table 1. **Conditions for the synthesis of specimens**

Specimen	Electrodes	t, °C	Note
R1	Fe	20	Specimen R4 was synthesized similarly to specimen R3, but at a larger surface area ratio between the Zn and Fe electrodes
R2	Fe	93	
R3	Fe + Zn	93	
R4	Fe + Zn	93	
R5	Zn	98	

The analysis of the calculation results showed that in the diffractograms of specimens R1 and R2 obtained using iron electrodes (Fig. 1, curves *a* and *b*, respectively), only reflections characteristic of magnetite were present. The calculation and experimental results are compared in Table 2. When calculating the angular positions of reflections, the known interplanar distances in magnetite [15, 16] were used. Table 2 does not include experimental results for magnetite reflections (111), (531), (620), (533), (622), and (444) because of their low intensity; therefore, they were not used in further calculations.

Table 2. **Comparison of calculation and experimental results for magnetite**

Calculation				Experiment	
hkl	*d*, nm	2θ	*I*, %	2θ	*I*, %
111	0.484	18.3	8	–	–
220	0.2967	30.1	30	30.3	33
311	0.2532	35.5	100	35.5	100
222	0.2424	37.1	8	–	–
400	0.2099	43.1	20	43.1	20
422	0.1715	53.4	10	53.6	8
511	0.1616	57.0	30	57.1	25
440	0.1485	62.5	40	62.5	43
531	0.1419	65.8	2	–	–
620	0.1328	71.0	4	–	–
533	0.1281	74	10	–	–
622	0.1266	75.0	4	–	–
444	0.1212	79.0	2	–	–

Table 3. **Comparison of calculation and experimental results for zinc ferrite**

Calculation				Experiment	
hkl	*d*, nm	2θ	*I*, %	2θ	*I*, %
111	0.484	18.3	20	–	–
220	0.298	30.0	50	30.0	43
311	0.253	35.5	100	35.3	100
222	0.243	37.0	10	–	–
400	0.21	43.1	40	42.9	18
422	0.172	53.3	40	53.3	34
511	0.162	56.8	40	56.7	59
440	0.149	62.3	80	62.5	36
531	0.133	70.9	20	–	–
620	0.128	74.1	40	–	–
533	0.127	74.8	10	–	–

The diffraction patterns of specimens R3 and R4 obtained when the iron and zinc electrodes were used simultaneously (Fig. 1, curves *c* and *d*, respectively) contain reflections with angular positions 2θ that are close to the angular positions of magnetite reflections, and reflections with new angular 2θ-positions (Fig. 1, curve *d*): $2\theta = 31.7°$, $34.4°$, $36.2°$, $47.5°$, $62.8°$, $66.3°$, $67.9°$, and $69.0°$. As shown in Refs. [17–19], these angular positions correspond to zinc oxide reflections with Miller indices (100), (002), (101), (102), (103), (200), (112), and (201), respectively. We did not use the zinc oxide reflection (110), for which $2\theta = 56.8°$, since its angular position practically coincides with the angular position of the (422) reflection of zinc ferrite. As a result, in the diffractograms of specimens R3 and R4 (Fig. 1, curves *c* and *d*, respectively), those two reflections overlap, and their integrated intensity considerably increases.

Analysis of the diffractogram of specimen R4 (Fig. 1, curve *d*) shows that the integrated intensity of zinc oxide reflections is substantially higher than that for specimen R3 (Fig. 1, curve *c*). Those two specimens were obtained using iron and zinc electrodes simultaneously. However, during the synthesis of specimen R4, the surface area of the zinc electrodes was larger than that during the synthesis of specimen R3. In our electrolytic synthesis method, the electrodes are the source of metal cations. Hence, the concentration of the latter is proportional to the electrode area. Therefore, in the case of a larger surface area of electrodes, a larger number of Zn^{+2} cations arises, from which zinc ferrite and zinc oxide are formed. In both cases, the area of the iron electrodes was the same, and therefore, it was the excess of zinc ions that formed zinc oxide.

The experimental angular positions of the reflections in the diffractogram of specimen R3 (Fig. 1, curve *c*) were compared with the calculated angular positions of zinc ferrite reflections. The results of this comparison are given in Table 3. A comparison of the results presented in Tables 2 and 3 shows that the angular positions of the magnetite and zinc ferrite reflections are close.

One of the tasks solved by X-ray structural analysis is the determination of crystal lattice parameters. For this purpose, the Wolf–Bragg formula, the quadratic forms of the syngonies, and the angular positions of the reflections in the X-ray diffraction patterns are used. The accuracy of this method is low, as a re-

sult of systematic and random errors. At the same time, some problems, such as the study of the nature of chemical bonding in solids and the determination of the characteristics of solid solutions, residual mechanical stresses, density, and the coefficient of thermal expansion, require exact values of the lattice parameters [20]. For the precise determination of the parameters, extrapolation or analytical methods are applied. Since systematic errors tend to zero at $\theta = 90°$, the function $\cos 2\theta$ is used as the extrapolating function, although it is nonlinear over a wide angular interval.

Both zinc ferrite and magnetite crystallize in a cubic system, space group No. 227 $Fd\bar{3}m$ (O_h^7 according to Schönflies notation). Therefore, by using the Wolf–Bragg formula and the quadratic form for the cubic system, we can calculate the value of the unit cell parameter d_2,

$$\frac{1}{d_2} = \frac{h_2 + k_2 + l_2}{a_2},$$

where a is the crystal lattice parameter, and h, k, and l are the Miller indices. As an extrapolation function, we used the function proposed by Riley, Nelson, Taylor, and Sinclair, which is considered the best extrapolation function [21],

$$f(\theta) = 0.5\left(\frac{\cos 2\theta}{\sin\theta} + \frac{\cos 2\theta}{\theta}\right).$$

Figure 2 illustrates the application of the extrapolation method to the determination of the crystal lattice parameter for a zinc ferrite specimen synthesized at a temperature of 93 °C. In this way, the values of the crystal lattice parameter were obtained for all studied specimens. As a result of the calculations, the following a-parameter values were determined for magnetite specimens obtained at different temperatures: $a = 0.8391$ nm at 93 °C, and $a = 0.8384$ nm at 20 °C. These results are close to the values of the magnetite lattice constant obtained by other authors [16, 22, 23]. For specimens synthesized using iron and zinc electrodes, the following values of the lattice constant were obtained: $a = 0.8454$ nm for specimen R3 and $a = 0.8465$ nm for specimen R4 (the diffraction patterns obtained for specimens R3 and R4 are shown in Fig. 1, curves c and d, respectively). These values correspond to the crystal lattice parameter of iron ferrite obtained by the authors of

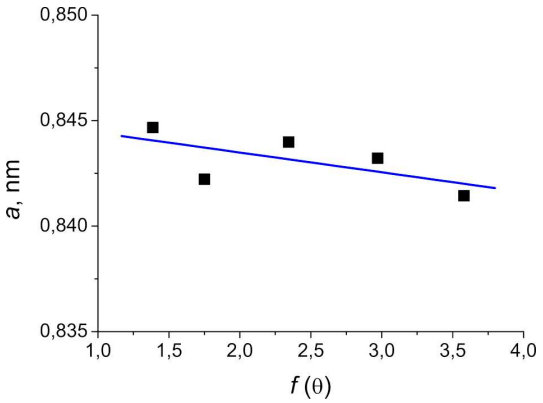

Fig. 2. Graphical extrapolation for determining the crystal lattice parameter of zinc ferrite nanocrystals synthesized at a temperature of 93 °C. The corresponding diffractogram is shown in Fig. 1 (curve *c*, iron and zinc electrodes)

Refs. [7, 24, 25]. Thus, if iron electrodes are used, synthetic magnetite is obtained, whereas if iron and zinc electrodes are used simultaneously, zinc ferrite and zinc oxide are obtained.

The results obtained while processing experimental diffractograms were used to calculate the sizes of nanocrystals using the Debye–Scherrer formula [18]

$$D = \frac{0.89\lambda}{\beta\cos\theta},$$

where λ is the wavelength of X-ray radiation, β is the reflection half-width, and θ is the diffraction angle. The physical value of the half-width β was calculated using the formula

$$\beta = \sqrt{\beta_1^2 - \beta_2^2},$$

where β_1 is the experimental value of the X-ray reflection half-width, and β_2 is the corresponding instrumental value. The latter was determined by analyzing the X-ray diffraction patterns of standard silicon and Al_2O_3 powders obtained under the same conditions.

To determine the sizes of nanocrystals using the Debye–Scherrer method, six intense magnetite reflections were used: (220), (311), (400), (422), (511), and (440). The arithmetic mean nanoparticle size was 24.5 nm for specimen R1 synthesized at a temperature of 20 °C, and 34.0 nm for specimen R2 obtained at a temperature of 93 °C.

Similar results were obtained in Refs. [26, 27]. The authors of Ref.[27] obtained magnetite nanoparticles

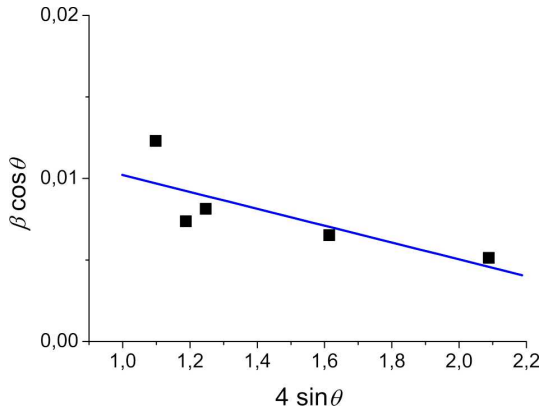

Fig. 3. Application of the Williamson–Hall method to $ZnFe_2O_4$ nanocrystals. The corresponding diffractogram is shown in Fig. 1 (curve *c*)

by simultaneously precipitating iron salts according to the reaction

$$Fe^{+2} + 2Fe^{+3} + 8NH_4OH = Fe_3O_4 + 4H_2O + 8NH_4^+.$$

The obtained specimens were studied by X-ray diffraction (XRD) and infrared (IR) spectroscopy. The nanoparticle sizes were determined using the Debye–Scherrer formula by analyzing the X-ray reflection with the maximum intensity. The obtained values were 10–12 nm. The diffractograms also registered Fe_2O_3 reflections with insignificant intensity. In Refs. [26, 27], solutions of $FeCl_3$, $FeCl_2$, and NH_4OH hydroxide in distilled water were used to synthesize Fe_3O_4. The synthesis was performed at a temperature of 85 °C and at pH = 11.0. The XRD and transmission microscopy (TEM) methods showed that the nanoparticle size was 10 nm.

To determine the size of iron ferrite nanocrystals, reflections (220), (311), (400), (511), and (440) were used. The arithmetic mean size value obtained for those reflections was 18.4 nm for specimen R3 and 15.1 nm for specimen R4; the corresponding diffractograms are shown in Figs. 1, *c* and 1, *d*, respectively. The arithmetic mean sizes of zinc oxide nanocrystals in those specimens were 8.9 and 38.8 nm, respectively.

The application of the Debye–Scherrer formula is based on the dependence of the X-ray reflection half-width on the particle size: as the particle size decreases, the half-width increases. It is also known that the half-width is affected by mechanical stresses that arise due to the presence of defects in the crystal lattice. For nanoparticles, such defects can manifest themselves because of a substantial fraction of atoms located on their surface, with the contribution of surface atoms increasing as the particle size decreases. Therefore, to determine the size and mechanical stresses acting in Fe_3O_4 nanocrystals, we used the Williamson–Hall method [28]. In this method, the reflection half-width is determined as the sum of two factors, dimensional and deformational,

$$\beta = \frac{0.89\lambda}{D\cos\theta} + 4\varepsilon\tan\theta,$$

where λ is the X-ray radiation wavelength, and ε is the relative elongation. In this formula, the first term corresponds to the contribution of the dimensional effect, and the second term to the contribution of mechanical stresses. Assuming that mechanical stresses are isotropic, this formula can be written in the form

$$\beta\cos\theta = \frac{0.89\lambda}{D} + 4\varepsilon\sin\theta.$$

By plotting this relation in the coordinate system $4\sin\theta$ vs $\beta\cos\theta$, a straight line is obtained from which the nanocrystal size D and the relative elongation ε can be determined (see Fig. 3).

In this way, the following values of the nanocrystal size D were obtained for zinc ferrite specimens R3 and R4, the diffraction patterns of which are shown in Fig. 1 (curves *c* and *d*, respectively): $D = 8.9$ nm, $\varepsilon = -0.0052$ and $D = 19.2$ nm, $\varepsilon = 5.3 \times 10^{-5}$, respectively. The minus sign of the relative elongation value indicates the compressive strain, and the plus sign indicates the tensile strain. From the obtained results, it is clear that an increase in the relative concentration of zinc cations in the electrolyte leads to the growth of $ZnFe_2O_4$ nanocrystals and changes in the type of their deformation.

According to Hooke's law, the mechanical stress under elastic deformation equals

$$\sigma = E\varepsilon,$$

where E is Young's modulus. Having determined the relative elongation from Hooke's law, we obtain the following relation

$$\beta\cos\theta = \frac{0.89\lambda}{D} + \frac{4\sigma\sin\theta}{E}.$$

By plotting this relation in the coordinate system $\frac{4\sin\theta}{E}$ vs $\beta\cos\theta$, a straight line is obtained from which the nanocrystal size D and the mechanical stress σ can be determined. For single-crystalline bodies, Young's modulus depends on the direction in the single crystal, i.e., on the values of the Miller indices $(h\,k\,l)$ and the crystal system type. For ZnO, which belongs to the hexagonal system, this dependence is described by the formula [29]

$$E^{-1} = [(h_2 + k_2 - hk)^2 a^4 s_{11} + l^4 c^4 s_{33} + \\ + (h_2 + k_2 - hk) l^2 a^2 c^2 (s_{44} + 2s_{13})]/ \\ /\{[(h^2 + k^2 - hk)a^2 + l^2 c^2]^2\},$$

where s_{11}, s_{13}, s_{33}, and s_{44} are the elastic compliance coefficients, and a and c are the parameters of the ZnO unit cell. Using the known values of the elastic compliance coefficients, the unit cell parameters [30] of zinc oxide, and the Miller indices of the reflections observed in the experimental diffractograms, we calculated Young's modulus for the corresponding reflections.

Figure 4 demonstrates an example of how the Williamson–Hall method is applied to determine the unit cell parameters for zinc oxide nanocrystals in specimens synthesized at a temperature of 93 °C. It can be seen that the experimental points deviate from a straight line. To obtain reliable values of the quantity $\frac{0.89\lambda}{D}$ and the mechanical stress σ, the least squares method was used. As a result, for the $ZnFe_2O_4$ and ZnO specimens (their diffraction patterns are shown in Fig. 1, curves c and d, respectively), the following values of the nanocrystal size D and the mechanical stress σ were obtained: $D =$ $= 8.9$ nm, $\sigma = -7.1 \times 10^8$ Pa and $D = 38.5$ nm, $\sigma = 7.8 \times 10^7$ Pa, respectively. It can be seen that, similarly to iron ferrite, as the synthesis temperature increases, the size D grows and the deformation type of ZnO nanocrystals changes.

The Raman scattering (RS) spectra of the examined specimens are shown in Fig. 5. From curves a and b, it can be seen that the spectra of magnetite synthesized at temperatures of 93 and 20 °C (R1 and R2, respectively) are practically identical. They contain scattering bands at frequency positions of 358, 671, 1133 (a shoulder), and 1344 cm^{-1}; the corresponding values of their half-widths are practically identical. The authors of Refs. [31–33] studied natural single-crystalline magnetite or powder prepared from

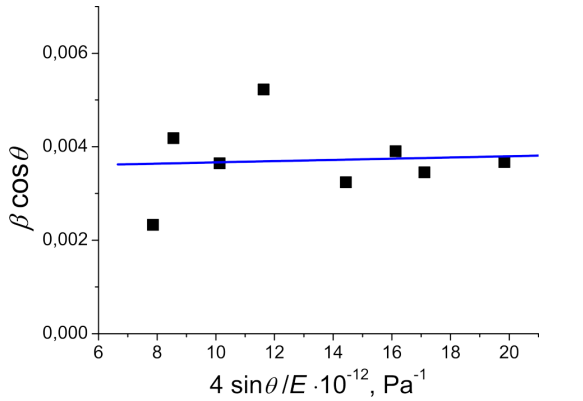

Fig. 4. Application of the Williamson–Hall method to ZnO nanocrystals. The corresponding diffractogram is shown in Fig. 1 (curve d)

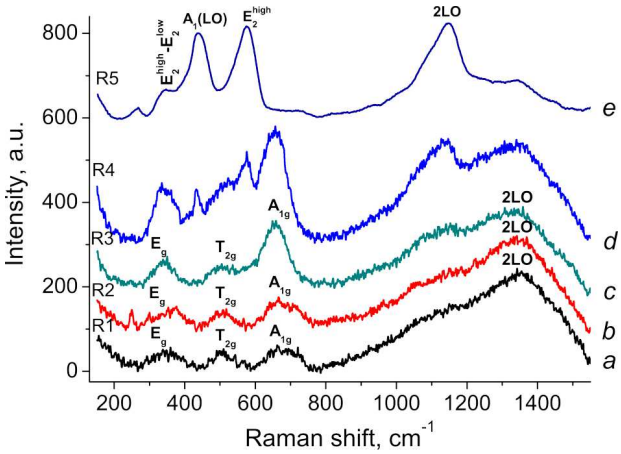

Fig. 5. Raman spectra of examined specimens: (a) specimen R1, zinc ferrite, $t = 20$ °C, Fe electrodes; (b) specimen R2, zinc ferrite, $t = 93$ °C, Fe electrodes; (c) specimen R3, "zinc ferrite–zinc oxide" system, $t = 93$ °C, Fe + Zn electrodes; (d) specimen R4, "zinc ferrite–zinc oxide" system, $t = 93$ °C, Fe + Zn electrodes; (e) specimen R5, zinc oxide, $t = 99$ °C, Zn electrode. The modes are shown (a, b, c) for zinc ferrite, (e) for zinc oxide

natural magnetite. They used laser radiation with a wavelength of 514.5 nm to study the Raman spectra. The following modes were registered: T_{2g} (at 193, 450–490, and 538 cm^{-1}), E_g (at 306 cm^{-1}), and A_{1g} (at 668 cm^{-1}). The broad band at 1330 cm^{-1} was identified as the second-order scattering spectrum.

An X-ray structural analysis showed that specimens R3 and R4, the Raman spectra of which are shown in Fig. 5 (curves c and d, respectively), consisted of iron ferrite and zinc oxide. Therefore, a

control specimen R5 was synthesized using the electrolytic method; it consisted only of ZnO nanocrystals. Curve *e* in Fig. 5 shows the Raman spectrum of zinc oxide nanocrystals obtained by the electrolytic method at an electrolyte temperature of 98 °C. The size of nanocrystals determined by the Debye–Scherrer method was 30.3 nm, and that determined by the Williamson–Hall method was 94.0 nm. The spectrum contains intense scattering bands at frequency positions of 344, 435, 574, 1134, and 1355 cm^{-1}. Comparing these results with the literature data [34–37], we may conclude that the first three bands belong to the active phonons at the center of the Brillouin zone: $E_2^{(high)} - E_2^{(low)}$, $A_1(TO)$, and $E_2^{(high)}$, respectively. The broad scattering band at the frequency position $\nu = 1134$ cm^{-1} is most likely a combination of 2LO, $2A_1(LO)$, and $2E_1(LO)$ phonons at highly symmetrical points of the Brillouin zone. The broad band at the frequency position $\nu = 1355$ cm^{-1} arises due to the presence of uncontrolled impurities and defects. Our data concerning the frequency positions differ from the corresponding values given in the literature [34–37], which may be associated with differences in the studied objects and the wavelengths of the light sources used for the excitation of Raman spectra. For example, the authors of Ref. [34] studied single-crystalline zinc oxide and obtained Raman spectra excited at a wavelength of 514.5 nm. In Ref. [35], the spectra were excited at a wavelength of 532 nm, and the studied object was nanocrystalline zinc oxide with crystallite sizes of 12–14 nm.

The Raman spectra of specimens R3 and R4 are shown in Fig. 5 (curves *c* and *d*, respectively); actually, they are superpositions of the $ZnFe_2O_4$ and ZnO spectra. A comparison of the Raman spectra of specimens R3–R5 (Fig. 5, curves *c*, *d*, and *e*, respectively) confirms the conclusion drawn from the analysis of diffractograms that the specimens contained different zinc oxide contents. The scattering bands in the $ZnFe_2O_4$ and ZnO spectra occurred at close frequency positions (Fig. 5, curve *d*); therefore, they were resolved into components using the Cauchy–Lorentz function. As a result, the following frequencies of scattering bands were obtained: 343, 434, 507, 572, and 655 cm^{-1}, with the scattering bands at frequency positions of 434 and 572 cm^{-1} belonging to zinc oxide. A comparison with the literature data [24, 38] made it possible to conclude that the scattering bands at 343, 507, and 655 cm^{-1} belong to the E_g, F_{2g}, and A_{1g} modes, respectively.

4. Conclusions

1) The electrolytic method makes it possible to obtain magnetite nanocrystals using iron electrodes and a sodium chloride solution as the electrolyte.

2) Magnetite nanocrystals synthesized at room temperature had smaller sizes than those synthesized at a temperature of 98 °C, and they were characterized by lower compressive mechanical stresses.

3) The simultaneous application of iron and zinc electrodes led to the synthesis of nanocrystals of the "zinc ferrite–zinc oxide" system.

4) The angular positions of reflections for magnetite and zinc ferrite are close; therefore, for an unambiguous identification of these compounds, it is preferable to determine the crystal lattice parameter.

1. L.D. Didukh. *Electricity and Magnetism* (Pidruchnyky i posobnuky, 2020) (in Ukrainian).
2. V.S. Bushkova. Structure and optical properties of nickel-cobalt ferrites obtained by the sol–gel method with autocombustion. *Zh. Nano-Elektron. Fiz.* **7**, 03021 (2015) (in Ukrainian).
3. O.I. Tovstolytkin, M.O. Borovyi, V.V. Kurylyuk, Yu.A. Kunytsky. *Physical Foundations of Spintronics* (Nilan-LTD, 2014) (in Ukrainian).
4. I. Zarandona, D.M. Correia, J. Moreira, C.M. Costa S. Lanceros-Mendez, P. Guerrero, K. de la Caba. Magnetically responsive chitosan-pectin films incorporating Fe_3O_4 nanoparticles with enhanced antimicrobial activity. *Int. J. Biol. Macromol.* **227**, 1070 (2023).
5. Yu.M. Poplavko. *Solid State Physics: Textbook. In 2 volumes* (Politekhnika, 2017) (in Ukrainian).
6. P. Pietrzyk, N.T. Phuong, S.J. Olusegun, N. Hong Nam, D.T.M. Thanh, M. Giersig, P. Krysiski, M. Osial. Titan yellow and congo red removal with superparamagnetic iron-oxide-based nanoparticles doped with zinc. *Magnetochemistry* **8**, 91 (2022).
7. Changwa Yao, Q.s Zeng, G. Goya, T. Torres, Jinfang Liu, Haiping Wu, Mingyuan Ge, Yuewu Zeng, Youwen Wang, J.Z. Jiang. $ZnFe_2O_4$ nanocrystals: Synthesis and magnetic properties. *J. Phys. Chem. C* **111**, 12274 (2007).
8. A. Karamipour, P.K. Parsi, P. Zahedi, S.M.A. Moosavian. Using Fe_3O_4-coated nanofibers based on cellulose acetate/chitosan for adsorption of Cr(VI), Ni(II) and phenol from aqueous solutions. *Int. J. Biol. Macromol.* **154**, 1132 (2020).
9. E. Bazrafshan, L. Mohammadi, A.A. Zarei, J. Mosafer, M. Zafar, A. Dargahi. Optimization of the photocatalytic degradation of phenol using superparamagnetic iron oxide

(Fe_3O_4) nanoparticles in aqueous solutions. *RSC Adv.* **13**, 25408 (2023).
10. W. Wang, Q. Mao, H. He, M. Zhou. Fe_3O_4 nanoparticles as an efficient heterogeneous Fenton catalyst for phenol removal at relatively wide pH values. *Water Sci. Technol.* **68**, 2367 (2013).
11. Juanli Shen, Yiming Zhou, Shengshi Li, Pengkun Gu, Guoxin Xue. Hydrogel-coated Fe_3O_4 nanoparticles as an efficient heterogeneous Fenton catalyst for degradation of phenol. *J. Mater. Sci.* **54**, 10684 (2019).
12. P.P. Gorbyk. Nanocomposites with functions of medical and biological nanorobots: synthesis, properties, applications. *Nanosyst. Nanomater. Nanotekhnol.* **11**, 0323 (2013) (in Ukrainian).
13. N.V.S. Vallabani, S. Singh. Recent advances and future prospects of iron oxide nanoparticles in biomedicine and diagnostics. *3 Biotech* **8**, 279 (2018).
14. Y.Y. Q. Meng, Y.N. Shi, Y.P. Zhu, Y.Q. Liu, L.W. Gu, D.D. Liu, A. Ma, F. Xia, Q.Y. Guo, C.C. Xu, J.Z. Zhang, C. Qiu, J.G. Wang. Recent trends in preparation and biomedical applications of iron oxide nanoparticles. *J. Nanobiotechnol.* **22**, 24 (2024).
15. P.I. Loboda, O.P. Karasevs'ka, I.Yu. Trosnikova. *X-ray Structural Analysis of Materials in a Dispersed State* (Tsentr Uchbovoi Literatury, 2017) (in Ukrainian).
16. V.O. Khmelevs'kyi, V.O. Dyakiv. *X-ray Determinant of Minerals* (LNU, 2014) (in Ukrainian).
17. V.R. Gaevs'kyi, B.D. Nechyporuk, M.Yu. Novoselets'kyi, B.P. Rudyk. Electrolytic method for obtaining zinc oxide nanoparticles. *Ukr. Fiz. Zh.* **58**, 385 (2013) (in Ukrainian).
18. B.P. Rudyk, B.D. Nechyporuk, M.Yu. Novoselets'kyi, V.A. Syas'kyi, B.A. Tataryn. Using the Williamson–Hall method to determine the size of ZnO nanoparticles. *Zh. Fiz. Dosl.* **19**, 1602 (2015) (in Ukrainian).
19. A.V. Lysytsya, M.V. Moroz, B.D. Nechyporuk, B.P. Rudyk, B.F. Shamsutdynov. Physical properties of zinc compounds obtained by the electrolytic method. *Fiz. Khim. Tverd. Tila* **22**, 160 (2021) (in Ukrainian).
20. S.I. Mudryi, Yu.O. Kulyk, A.S. Yakymovych. *X-ray Structural Snalysis in Materials Science* (LNU, 2017) (in Ukrainian).
21. H. Lipson, H. Steeple. *Interpretation of X-ray Powder Diffraction Patterns* (Macmillan, 1970).
22. A. Gholizadeh. Structural and mechanical properties of AFe_2O_4 ($A = Zn$, $Cu_{0.5}Zn_{0.5}$, $Ni_{0.3}Cu_{0.2}Zn_{0.5}$) nanoparticles prepared by citrate method at low temperature. *J. Am. Ceram. Soc.* **100**, 3577 (2017).
23. T. Heng, W. Ze, T. Wen-Sheng, L. Xiao-Ping, Q. Jian-Guo, Y. Xiao-Hong. Synthesis of magnetic Fe_3O_4 micro/nanospheres in organic solvent. *J. Appl. Biomat. Funct. Mater.* **16**, 26 (2018).
24. M.V. Nikolic, Z.Z. Vasiljevic, M.D. Lukovic, V.P. Pavlovic, J.B. Krstic, J. Vujancevic, N. Tadic, B. Vlahovic, V.B. Pavlovic. Investigation of $ZnFe_2O_4$ spinel ferrite nanocrystalline screen-printed thick films for application in humidity sensing. *Int. J. Appl. Ceram. Technol.* **16**, 981 (2019).
25. A. Pradeep, P. Priyadharsini, G. Chandrasekaran. Structural, magnetic and electrical properties of nanocrystalline zinc ferrite. *J. Alloys Compd.* **509**, 3917 (2011).
26. V.A.J. Silva, P.L. Andrade, M.P.C. Silva, A.G. Bustamante Dominguez, L.De Los Santos Valladares, J. Albino Aguiar. Synthesis and characterization of Fe_3O_4 nanoparticles coated with fucan polysaccharides. *J. Magn. Magn. Mater.* **343**, 138 (2013).
27. P.P. Gorbyk, N.V. Kusyak, A.L. Petranovskaya, E.I. Oranskaya, N.V. Abramov, N.M. Opanashchuk. Synthesis and properties of magnetic nanostructures with carbonized surface. *Khim. Fiz. Tehnol. Poverhn.* **9**, 176 (2018).
28. V.D. Mote, Y. Purushotham, B.N. Dole. Williamson-Hall analysis in estimation of lattice strain in nanometer-sized ZnO particles. *J. Theor. Appl. Phys.* **6**, 6 (2012).
29. P. Bindu, S. Thomas. Estimation of lattice strain in ZnO nanoparticles: X-ray peak profile analysis. *J. Theor. Appl. Phys.* **8**, 123 (1014).
30. A. Sadao. *Handbook on Physical Properties of Semiconductors. Vol. 3* (Kluwer, 2004).
31. O.N. Shebanova, P. Lazor. Raman spectroscopic study of magnetite ($FeFe_2O_4$): A new assignment for the vibrational spectrum. *J. Solid State Chem.* **174**, 424 (2003).
32. O.N. Shebanova, P. Lazor. Raman study of magnetite (Fe_3O_4): Laser-induced thermal effects and oxidation. *J. Raman Spectrosc.* **34**, 845 (2003).
33. M. Hanesch. Raman spectroscopy of iron oxides and (oxy)hydroxides at low laser power and possible applications in environmental magnetic studies. *Geophys. J. Int.* **177**, 941 (2009).
34. R. Cusco, E. Alarcon-Llado, J. Ibanez, L. Artus, J. Jimenez, B. Wang, M.J. Callahanet. Temperature dependence of Raman scattering in ZnO. *Phys. Rev. B* **75**, 165202 (2007).
35. O. Smirnov, V. Dzhagan, M. Kovalenko, O. Gudymenko, V. Dzhagan, N. Mazur, O. Isaieva, Z. Maksimenko, S. Kondratenko, M. Skorykde, V. Yukhymchuk. ZnO and Ag NP-decorated ZnO nanoflowers: green synthesis using Ganoderma lucidum aqueous extract and characterization. *RSC Adv.* **13**, 1 (2023).
36. J. de O. Primo, D.F. Horsth, J. de S. Correa, A. Das, C. Bittencourt, P. Umek, A.G. Buzanich, M. Radtke, K.V. Yusenko, C. Zanette, F.J. Anaissi. Synthesis and characterization of Ag/ZnO nanoparticles for bacteria disinfection in water. *Nanomaterials* **12**, 1764 (2022).
37. A. Srithar, J.C. Kannan, T.S. Senthil. Preparation and characterization of Ag doped ZnO nanoparticles and its antibacterial applications. *J. Adv. Chem.* **13**, 6273 (2017).
38. L.I. Granone, A.C. Ulpe, L. Robben, S. Klimke, M. Jahns, F. Renz, T.M. Gesing, T. Bredow, R. Dillert, D.W. Bahnemann. Effect of the degree of inversion on optical properties of spinel $ZnFe_2O_4$. *Phys. Chem. Chem. Phys.* **20**, 28267 (2018).

Received 16.11.25.
Translated from Ukrainian by O.I. Voitenko

А.В. Лисиця, В.О. Мислінчук, М.В. Мороз, Б.Д. Нечипорук, Б.П. Рудик, С.В. Вірко

ОТРИМАННЯ І ФІЗИЧНІ ВЛАСТИВОСТІ МАГНЕТИТУ ТА ФЕРИТУ ЦИНКУ

Досліджено можливість отримання нанокристалів магнетиту та фериту цинку електролітичним методом. Синтез наночастинок відбувався в електролізері з залізними або залізними і цинковими електродами, заповненому розчином NaCl у воді. Проведені рентгеноструктурні дослідження використано для визначення елементного складу отриманих зразків, розмірів нанокристалів і параметрів кристалічної ґратки. Розміри нанокристалів визначалися за допомогою формули Дебая–Шеррера, методу Вільямсона–Холла й розмірно-деформаційного методу. Показано, що при використанні залізних електродів отримуються нанокристали магнетиту, а у випадку залізних і цинкових електродів отримується система "ферит цинку–оксид цинку". Проаналізовано спектри комбінаційного розсіяння світла досліджуваних зразків.

Ключові слова: магнетит, ферит цинку, рентгеноструктурні дослідження, розміри наночастинок, формула Дебая–Шеррера, метод Вільямсона–Холла, параметр кристалічної ґратки, комбінаційне розсіяння світла.